metals

Article

Cu-Interlayer-Enhanced Flexible Porous Ni-B on Waste Polyester Fabric Electrode: Robust Electrocatalytic Performance Under Repeated Bending and Twisting

Guangya Hou *, Siqi Chen, Jianli Zhang, Qiang Chen and Yiping Tang *

College of Materials Science and Engineering, Zhejiang University of Technology, Hangzhou 310014, China; chsiqi47@163.com (S.C.); zhangjianli@zjut.edu.cn (J.Z.); cq415@zjut.edu.cn (Q.C.)
* Correspondence: houguangya@zjut.edu.cn (G.H.); tangyiping@zjut.edu.cn (Y.T.)

Abstract

The functional valorization of waste fabrics, particularly their conversion into flexible low-cost, high-performance electrodes, holds significant promise for resource sustainability and the development of advanced energy technologies. Here, a NiB/Cu/polyester fabric (PF) composite electrode was fabricated via two-step electroless plating on waste PF and was demonstrated as a bifunctional electrocatalyst for methanol oxidation (MOR) and urea oxidation (UOR). The morphology, crystal structure, surface chemical state, and wettability of the electrodes were characterized using SEM, TEM, XRD, XPS, and contact angle measurements. The Cu interlayer critically enhanced interfacial wettability, intrinsic catalytic activity and stability. At 0.8 V, the NiB/Cu/PF electrode delivered average current densities of 312 mA·cm^{-2} for MOR and 288 mA·cm^{-2} for UOR, outperforming NiB/PF by 27.9% and 9.1%, respectively. After 2000 accelerated degradation cycles with electrolyte renewal, MOR and UOR activities were retained at 91.6% and 105.0%, respectively. Remarkably, the Cu interlayer conferred exceptional mechanical–electrochemical robustness: following 100 sequential bending and twisting deformations, current density retention ranged from 84.6% to 96.7% across multiple test configurations. The Cu interlayer acted as a flexible stress buffer during mechanical deformation, effectively improving the adhesion between the coating and the substrate.

Keywords: methanol oxidation; urea oxidation; electrocatalysis; flexible electrode; interlayer

1. Introduction

With the acceleration of global population growth and industrial technology iteration, the energy system dominated by fossil fuels faces a dual crisis of resource depletion and environmental deterioration. Developing high-performance and low-cost fuel cell catalyst systems is of great strategic significance for building a green and low-carbon energy network [1,2]. Direct methanol fuel cells (DMFCs) and direct urea fuel cells (DUFCs) have attracted attention due to their high energy conversion efficiency, safe usage, storage and transportation, as well as economic and environmental benefits [3–6].

However, the large-scale application of DMFCs and DUFCs still faces key challenges. Currently, commercial applications mainly use high-cost precious metals such as Pt and their compounds as catalysts, and their scarcity and price volatility severely constrain the technical economy. In addition, the anode catalyst poisoning caused by methanol crossover in DMFCs and the slow kinetics of the urea oxidation reaction (UOR) in DUFCs further

Check for updates

Academic Editor: Henrik K Hansen

Received: 7 April 2026
Revised: 5 May 2026
Accepted: 8 May 2026
Published: 13 May 2026

Copyright: © 2026 by the authors. Licensee MDPI, Basel, Switzerland. This article is an open access article distributed under the terms and conditions of the Creative Commons Attribution (CC BY) license.

aggravate the system efficiency loss. Therefore, while searching for the preparation of high-performance Pt alternative catalysts, the choice of support material also plays an important role in catalytic activity [7,8].

Nickel-based materials have the characteristics of a Pt-like electronic structure, low cost, and abundant reserves. The combination with non-metals such as Ni-O, Ni-P, Ni-S, and Ni-B to form catalytic materials has attracted much attention for research on MOR and UOR. Compared with crystalline catalysts, Hu et al. [9] prepared a porous amorphous nickel–boron catalyst (a-NiBx) using a simple electroless plating method. The presence of B increased the adsorption energy of NiBx for urea molecules and hydroxyl ions, bringing the energy potential of NiBx closer to the thermoneutral value and significantly accelerating the kinetics of UOR. Huang et al. [10] synthesized a Ni-B electrocatalyst through a chemical reduction–annealing process. The ultrafine Ni-B nanoparticles had more active sites and higher activity. After annealing treatment, amorphous Ni-B transformed into crystalline Ni-B with lattice expansion, exhibiting a good electrocatalytic performance. Ni-B materials are promising electrocatalytic materials.

Rapid economic expansion and population growth have driven a substantial increase in global textile consumption—concurrently generating mounting volumes of post-consumer textile waste, which poses escalating environmental and resource management challenges [11–13]. Consequently, the recycling and functional valorization of waste fabrics represents not only a critical strategy for circular resource recovery but also a promising avenue for enabling sustainable energy technologies. Zhang et al. [14] constructed a self-supported nitrogen-doped carbon electrocatalyst using the thermal carbonization of waste silk fabric, which exhibited a unique porous three-dimensional (3D) structure that could expose more active sites and promote the efficient diffusion of the electrolyte. Jiang et al. [15] prepared an efficient oxygen evolution reaction (OER) catalyst with a metal and heteroatom co-doped carbon fiber structure using waste cotton fabric through a simple two-step carbonization process.

To make waste fabrics into conductive electrodes, high conductivity is typically achieved by coating the fabric surface with metals or metal salts [16,17]. Common conductive fabric manufacturing processes include electroplating [18,19], magnetron sputtering [20,21], chemical vapor deposition [22,23], sol–gel wet spinning [24], and electroless plating [25–28]. Among these techniques, electroless plating is favored due to its cost-effectiveness, simple process, ability to form a strong coating, and controlled uniform deposition on non-conductive fabric surfaces [29]. Wang et al. [30] deposited metal layers on various substrates such as cotton cloth, filter paper, and sponge via electroless plating to construct highly conductive flexible electrodes. These electrodes formed a continuous conductive network while maintaining the original three-dimensional porous structure and flexibility of the substrate, thus enabling successful application in flexible batteries. Khajeh et al. [31] prepared a Ni-P coating on nylon nonwoven fabric surfaces using electroless plating technology, obtaining a multifunctional conductive fabric with conductive and thermal response characteristics. This material achieved uniform coverage of the metal layer while maintaining the lightweight and breathable properties of the nonwoven fabric, thereby exhibiting various functions such as electromagnetic shielding, electrothermal and photothermal conversion. The above studies mainly focus on the construction and performance optimization of the metal coating itself, while the role of the metal interlayer in electrochemical performance remains underexplored. In this work, we demonstrate that the introduction of a Cu interlayer significantly enhances the interfacial wettability, intrinsic catalytic activity, and stability of the Ni-B-coated polyester fabric electrode. Moreover, the Cu interlayer confers exceptional mechanical–electrochemical robustness: it acts as a flexible stress buffer during mechanical deformation, effectively improving the adhesion

between the Ni-B coating and the fabric substrate, and enables the electrode to maintain a stable performance under repeated bending and twisting.

Despite the advantages of electroless plating, the influence of a metallic interlayer (e.g., Cu) on the catalytic performance of Ni-B-coated fabric electrodes has not been systematically investigated. In particular, the combined effects on wettability, charge transfer, and mechanical flexibility remain unexplored. Herein, we report a flexible NiB/Cu/polyester fabric (PF) electrode fabricated using a two-step electroless plating method. The role of the Cu interlayer is systematically evaluated, and the electrode is characterized by its morphology, wettability, and electrocatalytic activity toward MOR and UOR.

2. Materials and Methods

2.1. Materials and Chemicals

Polyester fabric was obtained from Sijiqing Old Clothing Market in Hangzhou, China. The waste polyester fabric is a woven satin fabric with a smooth surface. Its chemical composition is polyethylene terephthalate (PET). The average diameter of the polyester fibers is approximately 15 μm. Nickel chloride ($NiCl_2·6H_2O$, AR, ≥98%), stannous chloride ($SnCl_2·2H_2O$, AR), sodium hydroxide (NaOH, AR, ≥96%), copper sulfate ($CuSO_4·5H_2O$, AR, ≥99%), hydrochloric acid (HCl, AR, 36–38%), ammonia solution (NH_3, AR, 25–28%), formaldehyde solution (CH_2O, AR), potassium hydroxide (KOH, AR, 85%), methanol (CH_3OH, AR, ≥99.5%), and urea ($CO(NH_2)_2$, AR, 99%) were purchased from Sinopharm Chemical Reagent Co., Ltd. (Shanghai, China). Potassium sodium tartrate ($C_4H_4O_6KNa·4H_2O$, AR, ≥99%) and dimethylamine borane (DMAB, $C_2H_{10}BN$, ≥96%) were purchased from Aladdin, Ltd., Shanghai, China. Palladium chloride ($PdCl_2$, 59–60%) was purchased from Shuangmu Chemical Co., Ltd., Hangzhou, China.

2.2. Synthesis of Electrode Materials

2.2.1. Pretreatment of Polyester Fabric (PF)

Waste polyester fabric was cut into 1 cm × 2 cm strips, thoroughly rinsed with deionized water to remove surface contaminants, and dried at 60 °C under ambient atmosphere prior to use.

2.2.2. Synthesis of Cu/PF Electrodes

The pretreated PF was sequentially immersed in a sensitization solution containing $SnCl_2·2H_2O$ (44.3 mM) and HCl (0.50 M) and an activation solution containing $PdCl_2$ (2.82 mM) and HCl (0.50 M) at room temperature for 10 min each, followed by thorough rinsing with deionized water. Subsequently, electroless copper plating was performed at 45 °C for 60 min in a bath containing 0.03 M $CuSO_4·5H_2O$, 0.14 M $NaKC_4H_4O_6·4H_2O$, 0.1 M NaOH, and 0.13 M CH_2O. In this bath, $CuSO_4·5H_2O$ serves as the metal ion source, potassium sodium tartrate acts as a complexing agent to stabilize Cu^{2+} ions, NaOH adjusts the pH to an alkaline condition, and formaldehyde functions as the reducing agent for the electroless deposition of Cu. After rinsing and drying at 60 °C, the Cu/PF electrode was obtained. To optimize interfacial conductivity and catalytic support, copper plating duration was systematically varied (15, 30, 45, 60, and 75 min), yielding samples designated as Cu/PF-t15, Cu/PF-t30, Cu/PF-t45, Cu/PF-t60 (as Cu/PF), and Cu/PF-t75, respectively.

2.2.3. Synthesis of NiB/Cu/PF Electrodes

The as-prepared Cu/PF was further processed following a similar procedure. Cu/PF was sequentially immersed in the sensitization solution and activation solution at room temperature for 10 min each, followed by thorough rinsing with deionized water. Subsequent electroless Ni-B deposition was carried out at 30 °C for 45 min in a bath containing 0.19 M

$NiCl_2 \cdot 6H_2O$, 20 mM DMAB, and 0.59 M $NH_3 \cdot H_2O$. In this bath, $NiCl_2 \cdot 6H_2O$ provides Ni^{2+} ions, DMAB acts as the reducing agent, and $NH_3 \cdot H_2O$ serves both as a complexing agent for Ni^{2+} and as a pH adjuster to maintain an alkaline environment, which is essential for the reduction reaction. After rinsing with deionized water, the sample was dried at 60 °C to obtain NiB/Cu/PF. To tailor the catalytic electronic structure and surface reactivity, the DMAB concentration—and thus the nominal B content—was systematically varied from 5 to 25 mM in 5 mM increments (i.e., 5, 10, 17.5, 20, and 25 mM), yielding samples designated as 5-NiB/Cu/PF, 10-NiB/Cu/PF, 17.5-NiB/Cu/PF, 20-NiB/Cu/PF (as NiB/Cu/PF), and 25-NiB/Cu/PF, respectively.

For comparative evaluation, the NiB/PF control electrode was prepared by directly applying the identical Ni–B electroless deposition protocol to pristine polyester fabric (PF), omitting the Cu interlayer step. Figure 1 shows the synthesis process of the flexible NiB/Cu/PF electrode. The NiB/Cu/PF samples used for all characterizations in this work were prepared with a Cu plating time of 60 min and a DMAB concentration of 20 mM.

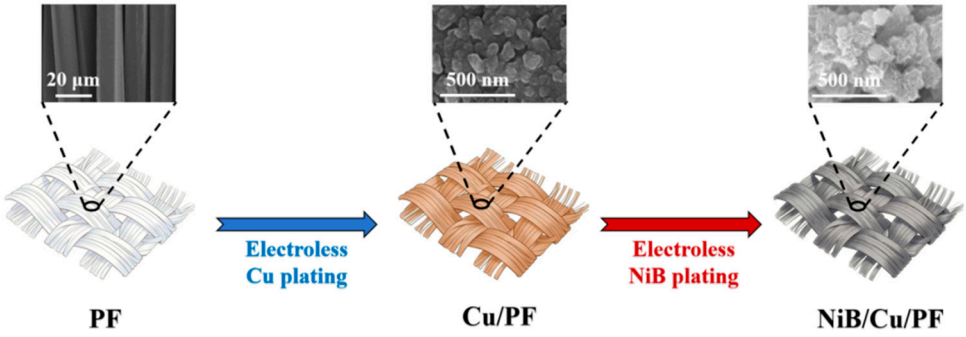


Figure 1. Schematic diagram of the preparation process of the NiB/Cu/PF electrode.

2.3. Material Characterization

The wettability of the samples was measured using a fully automatic optical contact angle measuring instrument (OCA30, Dataphysics, Filderstadt, Germany). The X-ray diffraction (XRD) patterns of the samples were characterized using an X-ray diffractometer (Bruker D8 Advance, Karlsruhe, Germany) with a Cu-Kα radiation source (λ = 1.546 Å) in the 2θ range of 20–80° at a scanning speed of $20° \cdot min^{-1}$ and a step size of 0.02°. The surface of the samples was chemically analyzed using X-ray photoelectron spectroscopy (XPS, Thermo Scientific K-Alpha, East Grinstead, UK). The micromorphology and crystal structure of the samples were characterized using field emission scanning electron microscopy (FEI Nano Nova 450, Brno, Czech Republic) and transmission electron microscopy (JEOL JEM F200,Tokyo, Japan). The chemical composition and elemental distribution were analyzed using high-angle annular dark-field scanning transmission electron microscopy (HAADF-STEM) coupled with energy-dispersive X-ray spectroscopy (EDS), performed on a JEOL JEM-F200 transmission electron microscope (JEOL Ltd., Tokyo, Japan).

Electrochemical performance was measured using a three-electrode system on an electrochemical workstation (CHI 760e, Chenhua Instruments, Shanghai, China). The prepared samples, Pt foil, and a saturated calomel electrode (SCE, E = 0.242 V vs. NHE) were used as the working electrode, counter electrode, and reference electrode, respectively, to evaluate the OER, MOR, and UOR performance. The catalytic performance was assessed using cyclic voltammetry (CV) at a scan rate of $50\ mV \cdot s^{-1}$ in 1.0 M KOH solution, 1.0 M KOH + 0.5 M CH_3OH solution, and 1.0 M KOH + 0.33 M $CO(NH_2)_2$ solution. Electrochemical impedance spectroscopy (EIS) was measured in the frequency range of 0.01 Hz to 100 kHz. The cycle life and long-term stability of the catalytic electrodes were evaluated using chronopotentiometry (CP) at $100\ mA \cdot cm^{-2}$ and 2000 cycles of cyclic voltammetry (CV).

The working electrode (1 cm × 2 cm sample) and a Pt foil counter electrode were placed parallel in the same beaker containing the electrolyte. The reference electrode was placed in a separate beaker with saturated KCl and connected via a salt bridge to the working electrode beaker. The immersion depth was adjusted to 1 cm using a ruler, defining a working electrode area of 1 cm^2. Although the fabric substrate is flexible, the deposited metal layer imparts sufficient rigidity to the electrode; in the electrolyte, the electrode remains straight and does not curl, ensuring a reproducible electrode/electrolyte interface. The schematic diagram of this configuration is shown in Figure S1.

3. Results and Discussion

3.1. XRD and XPS

Figure 2 shows the XRD patterns of the PF, Cu/PF, NiB/PF, and NiB/Cu/PF electrodes. Two broad diffraction peaks below 30° of 2θ are attributed to the weak carbon (C) peak of the amorphous polyester fabric (PF) substrate [32]. The Cu/PF electrode shows three dominant peaks at 2θ = 43.3°, 50.4°, and 74.1°, assigned to the (111), (200), and (220) planes of Cu (PDF#04-0836), with pronounced (111) intensity. The NiB/PF electrode exhibits three diffraction peaks at 2θ = 44.5°, 51.8°, and 76.4°, indexed to the (111), (200), and (220) planes of face-centered cubic (fcc) Ni, respectively (PDF#04-0850). Critically, the NiB/Cu/PF pattern integrates both sets of peaks—confirming the coexistence of crystalline Cu and Ni phases. Notably, the Ni diffraction peaks in both the NiB/PF and NiB/Cu/PF electrodes exhibit broadening and reduced intensity characteristic of low crystallinity and partial amorphous formation during electroless Ni–B deposition on PF substrates.

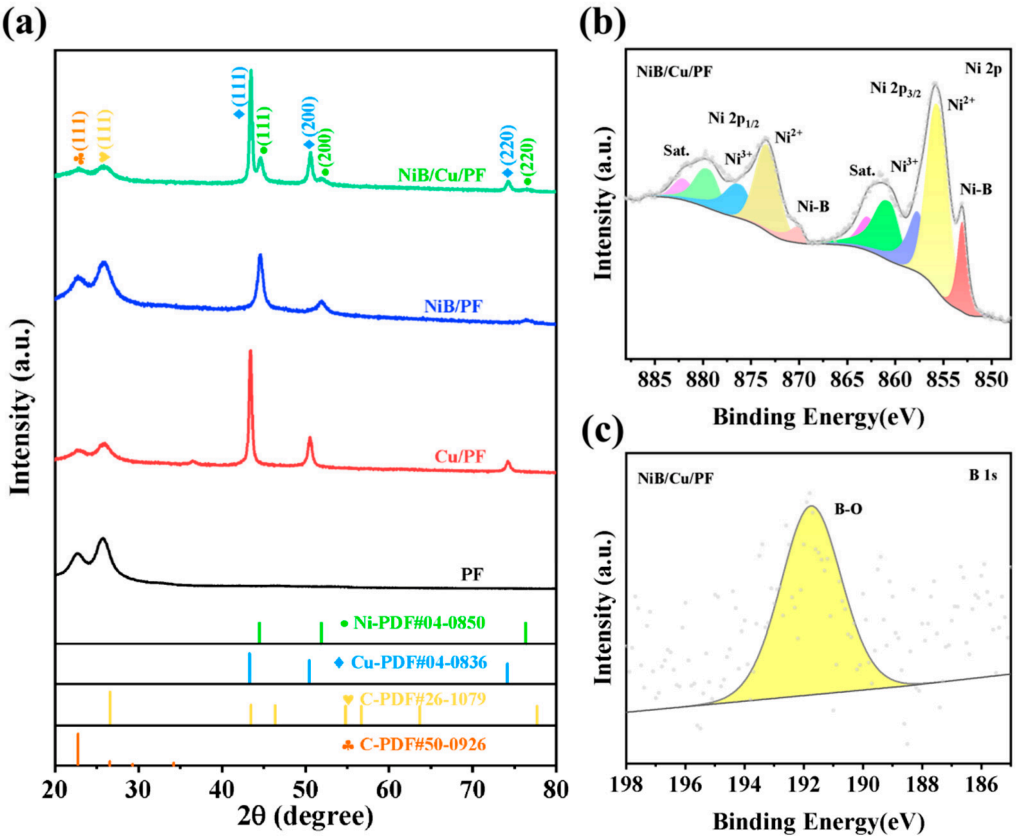


Figure 2. (**a**) XRD patterns of PF, Cu/PF, NiB/PF, and NiB/Cu/PF electrodes. High-resolution XPS spectrum of (**b**) Ni 2p. (**c**) B 1s.

The surface chemical state and elemental composition of the NiB/Cu/PF electrode were characterized using X-ray photoelectron spectroscopy (XPS). High-resolution spectra

of the Ni 2p and B 1s regions (Figure 2b,c) reveal characteristic binding energies consistent with Ni–B alloy formation. The Ni $2p_{3/2}$ peak at 853.1 eV is assigned to metallic Ni in the Ni–B matrix—distinct from the Ni^{2+} species core level of Ni $2p_{3/2}$ in Ni-B [33]. The broad shake-up satellites (marked as "Sat." in Figure 2b) at approximately 861 eV and 880 eV are characteristic of Ni^{2+} species, indicating the presence of a thin native oxide/hydroxide layer on the Ni–B surface [34]. In the B 1s spectrum, the peak at 191.8 eV corresponds to oxidized boron. The O 1s spectrum (Figure S2) exhibits a distinct peak at 531.3 eV, further corroborating the presence of a thin native oxide layer on the Ni–B surface. The atomic percentages of Ni, Cu, B, C, and O derived from XPS survey spectra are summarized in Table S2. Collectively, these results confirm the successful deposition of a Ni–B phase with mixed metallic and oxidized surface character.

3.2. Wettability

Wettability influences interfacial charge/mass transport in aqueous electrocatalytic systems. Contact angle measurements (Figure 3a–e) quantitatively assess the surface wettability of NiB/PF and NiB/Cu/PF electrodes in various electrolyte media, including KOH, methanol, and urea. Both electrodes exhibit markedly reduced contact angles upon addition of KOH to methanol or urea solutions, demonstrating enhanced hydrophilicity under alkaline conditions. This pronounced wettability improvement confirms effective electrolyte penetration and uniform electrode surface coverage, thereby validating the choice of alkaline mixed electrolytes for subsequent electrocatalytic performance evaluation.

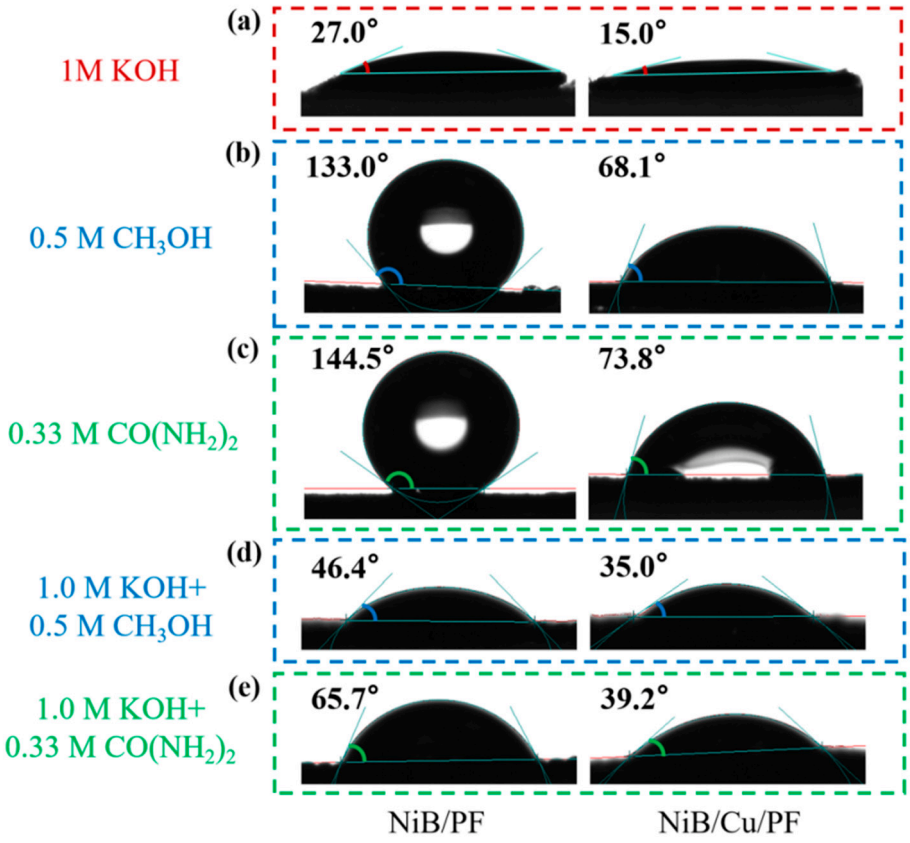


Figure 3. Initial contact angles of NiB/PF and NiB/Cu/PF electrodes in (**a**) 1.0 M KOH, (**b**) 0.5 M CH_3OH, (**c**) 0.33 M $CO(NH_2)_2$, (**d**) 1.0 M KOH + 0.5 M CH_3OH, (**e**) 1.0 M KOH + 0.33 M $CO(NH_2)_2$.

In methanol and urea solutions, the NiB/PF electrode exhibited larger contact angles, with minimal temporal variation and stable droplet morphology—indicative of poor surface hydrophilicity and limited electrolyte affinity. In contrast, the NiB/Cu/PF electrode showed

smaller contact angles in all test solutions, demonstrating excellent wettability, which is beneficial for the rapid diffusion of electrolyte ions and thus promotes the electrochemical reaction process [35].

3.3. Microstructure

The micromorphology of the Cu/PF, NiB/PF, and NiB/Cu/PF electrodes was characterized using scanning electron microscopy (SEM). As shown in Figure 4(a1,a2), small Cu particles are uniformly distributed across the PF fiber surfaces—forming a well-defined, continuous layer. The SEM images of the NiB/PF electrode (Figure 4(b1,b2)) reveal delicate flower-like nanospheres composed of thin, interconnected nanosheets, uniformly coating the fiber surface. In the NiB/Cu/PF electrode (Figure 4(c1,c2)), this elegant nanostructure is further enriched: the underlying Cu interlayer remains clearly visible, while the NiB nanosheets grow more densely and abundantly—resulting in significantly enhanced surface texture and microstructural complexity. This thoughtful architectural synergy between Cu and NiB not only preserves the structural integrity of the fibers but also increases surface roughness and effective area—offering more accessible active sites and supporting a stronger electrocatalytic performance. Finally, the cross-sectional SEM image (Figure 4d) of the NiB/Cu/PF sample clearly confirms the uniform presence and continuity of the Cu interlayer within the composite architecture.

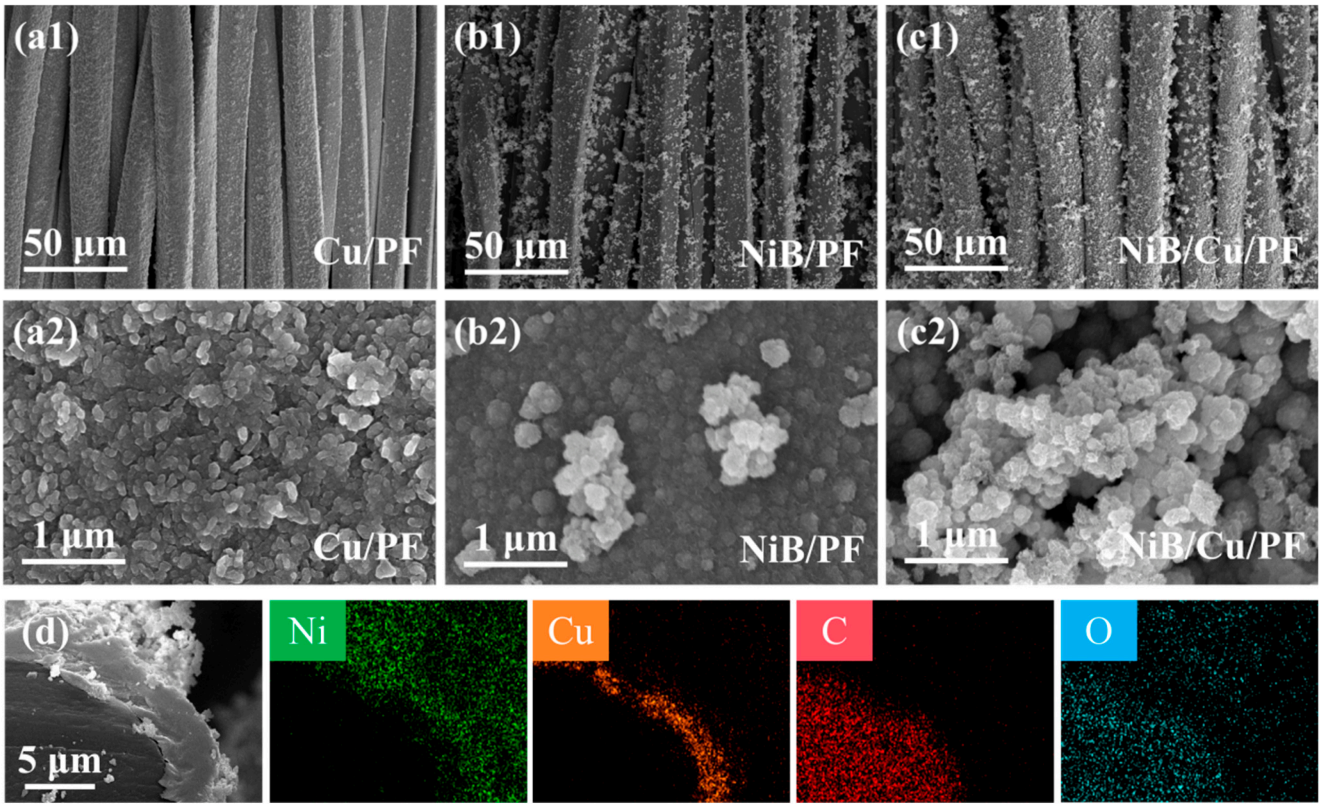


Figure 4. SEM images of (**a1**,**a2**) Cu/PF, (**b1**,**b2**) NiB/PF, (**c1**,**c2**) NiB/Cu/PF, (**d**) cross-section of NiB/Cu/PF fiber.

The micromorphology of the NiB/Cu/PF electrode was carefully examined using SEM and transmission electron microscopy (TEM). As shown in Figure 5a, the SEM image reveals a well-integrated, hierarchical surface architecture—where NiB nanosheets gracefully coat the underlying Cu-decorated PF fibers. The corresponding TEM image (Figure 5b) shows that the larger nanoparticles are uniformly enveloped by vertically aligned, ultrathin nanosheets. In Figure 5c, the coexistence of amorphous NiB regions and crystalline Ni

regions with clear lattice fringes can be clearly observed, together forming an amorphous–crystalline composite structure of NiB. Furthermore, the inverse fast Fourier transform (IFFT) images in Figure 5(c1,c2) show lattice fringes with spacings of 0.177 and 0.202 nm, corresponding to the (002) and (111) planes of Ni, respectively.

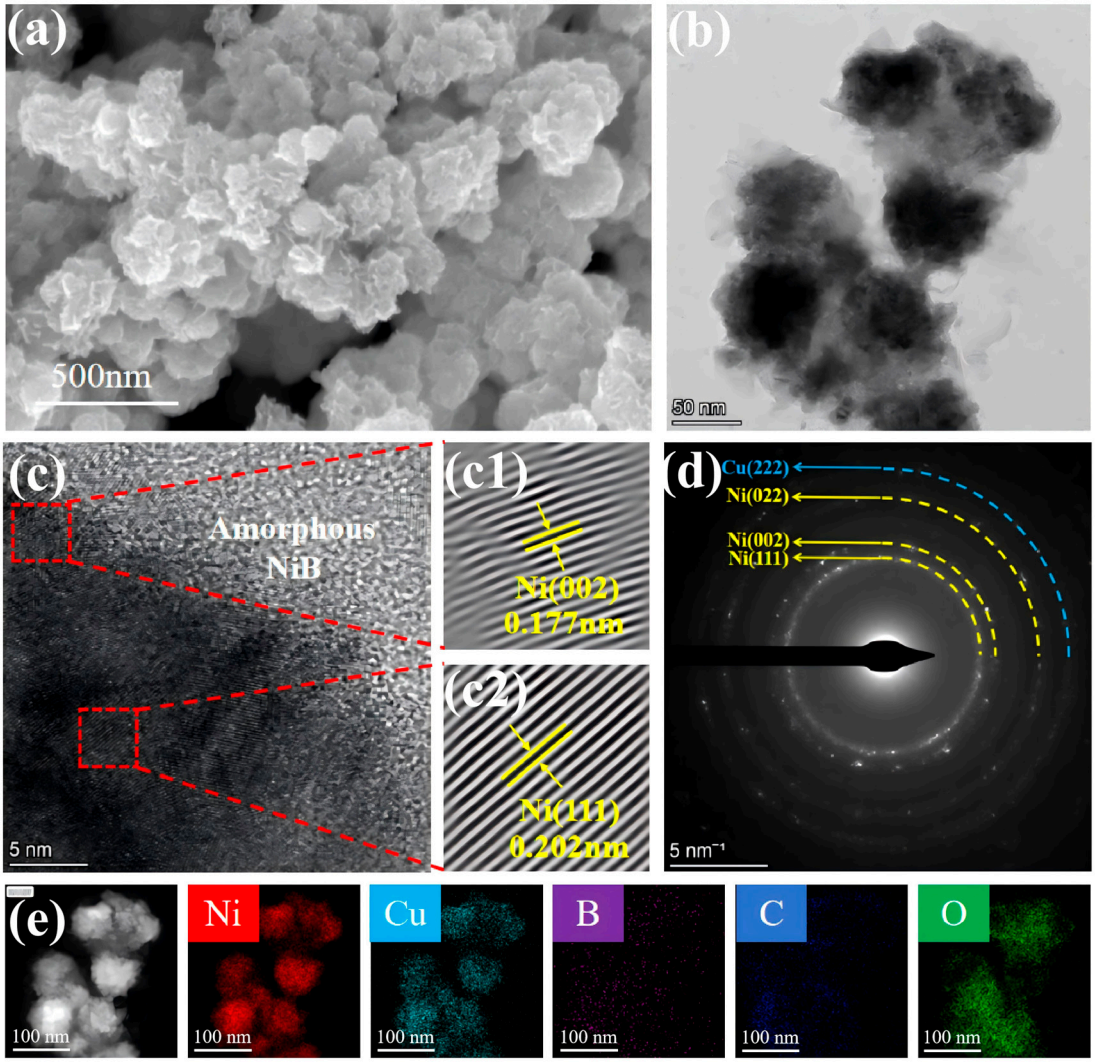


Figure 5. (**a**) SEM image, (**b**) TEM image, (**c**) HRTEM image, (**c1**,**c2**) IFFT images, (**d**) SAED pattern, (**e**) EDS elemental mapping images of NiB/Cu/PF.

The selected-area electron diffraction (SAED) pattern (Figure 5d) exhibits distinct polycrystalline diffraction rings: yellow rings indexed to the Ni (111), (002), and (022) lattice planes, and a blue ring assigned to the Cu (222) reflection—collectively confirming the coexistence of crystalline Ni and Cu phases. In addition, the high-angle annular dark-field scanning transmission electron microscopy (HAADF-STEM) image and corresponding elemental mapping images in Figure 5e show that Ni, Cu, B, C, and O elements are uniformly distributed, further confirming the successful incorporation of B.

3.4. Electrochemical Performance

The electrocatalytic performance of the prepared electrodes was tested using a three-electrode system at a scan rate of 50 $mV \cdot s^{-1}$. As shown in Figure 6a, Cu/PF exhibited no obvious oxidation peak in 1.0 M KOH solution. The CV curves of both NiB/PF and NiB/Cu/PF electrodes show distinct redox peaks, corresponding to the reversible conversion between Ni^{2+} and Ni^{3+} [36]. Compared with NiB/PF, the redox peak area of

NiB/Cu/PF increases, indicating improved electrochemical reversibility and enhanced accessibility of active sites, thereby enhancing the catalytic activity [37].

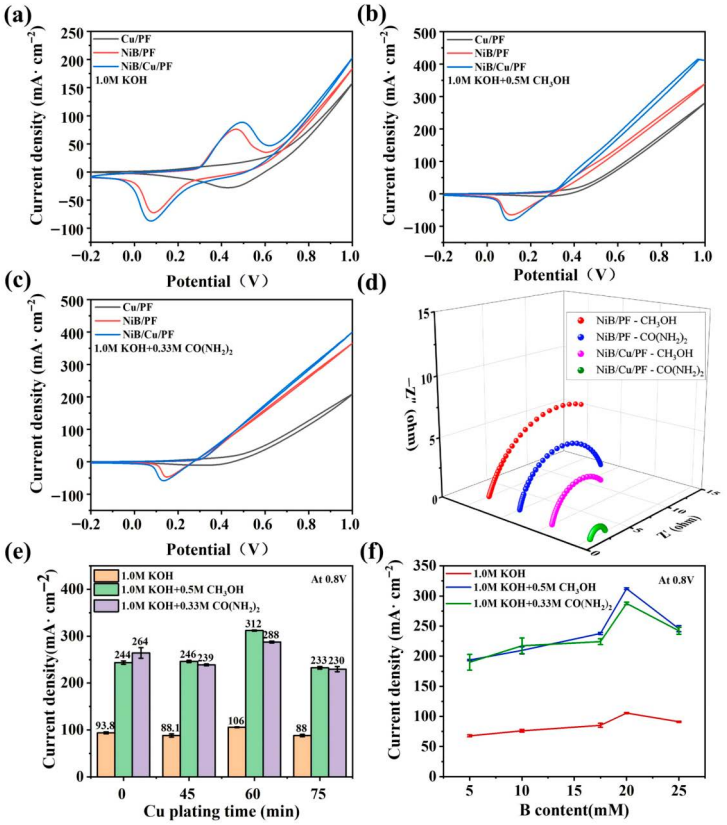


Figure 6. CV curves of different electrodes in (**a**) 1 M KOH, (**b**) 1.0 M KOH + 0.5 M CH_3OH, (**c**) 1.0 M KOH + 0.33 M $CO(NH_2)_2$. (**d**) EIS curves of NiB/PF and NiB/Cu/PF in 1.0 M KOH + 0.5 M CH_3OH and 1.0 M KOH + 0.33 M $CO(NH_2)_2$. (**e**) Peak current densities of NiB/Cu/PF electrodes with different electroless Cu plating times in different electrolytes at 0.8 V. (**f**) Peak current densities of NiB/Cu/PF electrodes with different B contents in different electrolytes at 0.8 V.

Figure 6b,c show the MOR and UOR performance of the two electrodes in 1.0 M KOH + 0.5 M CH_3OH and 1.0 M KOH + 0.33 M $CO(NH_2)_2$, respectively. The NiB/Cu/PF electrode exhibits significantly enhanced electrocatalytic activity. At a potential of 0.8 V, its average current densities are 312 mA·cm^{-2} for MOR and 288 mA·cm^{-2} for UOR, representing enhancements of 27.9% and 9.1%, respectively, relative to the NiB/PF. In addition, a comparison of the MOR and UOR performance with recently reported Ni-based (including flexible) electrodes (shown in Table S1) reveals that the NiB/Cu/PF electrode in this work exhibits a good performance. Figure 6d presents the electrochemical impedance spectroscopy (EIS) spectra of the NiB/PF and NiB/Cu/PF electrodes in two kinds of electrolytes. The fitted charge-transfer resistance (R_{ct}) values are 17.43 Ω for MOR and 10.45 Ω for UOR on NiB/PF, decreasing markedly to 7.02 Ω (MOR) and 1.77 Ω (UOR) on NiB/Cu/PF. This substantial reduction in R_{ct} was by 59.7% for MOR and 83.1% for UOR. This performance enhancement is ascribed to the Cu interlayer, which concurrently increases the density of electrochemically accessible active sites, reduces charge-transfer resistance, and accelerates interfacial charge-transfer kinetics. In 1.0 M KOH + 0.5 M CH_3OH, the double-layer capacitance (Cdl) of NiB/PF and NiB/Cu/PF are 1.25 and 3.26 mF·cm^{-2}, respectively, and the Tafel slopes are 91 and 69 mV·dec^{-1}. In 1.0 M KOH + 0.33 M $CO(NH_2)_2$, the Cdl values are 1.91 and 3.25 mF·cm^{-2}, and the Tafel slopes are 141 and 72 mV·dec^{-1}, respectively

(Figures S3 and S4). These results indicate that NiB/Cu/PF possesses a larger electrochemically active surface area and faster reaction kinetics than NiB/PF.

The effect of the Cu interlayer prepared with different electroless plating times on the performance of the NiB/Cu/PF electrode was investigated, and the results are shown in Figure 6e. The CV curves of Cu/PF electrodes with different electroless Cu plating times are shown in Figure S5. These curves show that the 60 min plating time yields the largest redox peak area, consistent with the current density trend in Figure 6e. The electrode fabricated with a copper plating duration of 60 min delivers the highest current density. With increasing plating time from 0 to 60 min, the Cu layer gradually forms a continuous conductive network, which is beneficial for improving electron transport capability and increasing the exposure of active sites. Beyond 60 min, with further extension to 75 min, the excessively thick Cu layer may cover part of the surface structure and reduce the effective specific surface area, leading to a decrease in current density [38].

In addition, the effect of boron (B) content in the electroless plating solution on the electrode performance was studied, and the results are shown in Figure 6f. The CV curves of NiB/Cu/PF electrodes with different B contents are shown in Figure S6. It can be seen that the sample with 20 mM DMAB exhibits the most pronounced redox peaks, which correlates well with the highest current density in Figure 6f. A series of samples were prepared by adjusting the B concentration to 5, 10, 17.5, 20, and 25 mM. With increasing B content, the current density of the electrode at 0.8 V first increases and then decreases. Increasing the boron precursor concentration from 17.5 mM to 20 mM markedly enhanced the catalytic activity for both MOR and UOR. However, further increasing the concentration to 25 mM led to a discernible decline in current density, indicating that 20 mM represents the upper bound of the optimal B-doping window under the given synthesis conditions. An appropriate amount of B can modulate the electronic structure of Ni and promote the formation of NiOOH active species, thereby increasing the electrocatalytic reaction rate. In contrast, excessive B incorporation induces thickening of the deposited layer or excessive structural disorder, which in turn affects electron transport and reactant diffusion, resulting in decreased catalytic performance [39].

3.5. Electrochemical Stability

Figure 7a,b show the chronopotentiometry (CP) curves of the two electrodes at a constant current density of 100 $mA \cdot cm^{-2}$. In the methanol oxidation reaction (MOR) electrolyte, both electrodes exhibited minimal potential drift over time. In contrast, during the urea oxidation reaction (UOR), both electrodes displayed a gradual positive potential shift accompanied by moderate fluctuations; nevertheless, the overall potential trajectories remained within a narrow, bounded range, confirming sustained electrocatalytic activity.

After identical testing durations, the potential retention values were 102.13% for NiB/PF and 99.79% for NiB/Cu/PF in MOR, and 110.04% for NiB/PF and 106.45% for NiB/Cu/PF in UOR. Notably, NiB/Cu/PF consistently operated at a lower overpotential and demonstrated a reduced potential fluctuation amplitude relative to NiB/PF across both systems, demonstrating that the Cu interlayer enhances not only intrinsic activity but also long-term potential stability under constant-current operation.

Figure 7c,d show the changes in current density at 0.8 V with the number of CV cycles up to 2000 cycles for the two electrodes. During the methanol oxidation reaction, the performance of both electrodes decreases within the first 2000 cycles. Following electrolyte replacement, the NiB/Cu/PF electrode recovered 91.61% of its initial current density for MOR, whereas NiB/PF recovered only 76.96%. A comparable recovery trend is observed for UOR: NiB/Cu/PF exhibits full activity restoration with a slight activation effect (105.00% of initial current density), while NiB/PF recovers to just 82.26%. The slight activation effect

(105.0% retention) for UOR after 2000 CV cycles is attributed to the in situ electrochemical reconstruction of the Ni–B surface during prolonged cycling. This reconstruction generates more NiOOH active species, leading to a slight enhancement of the urea oxidation activity. This indicates that NiB/Cu/PF exhibited superior cycling durability and electrochemical reversibility. The CV curves of the two electrodes before and after long-term cycling are shown in Figure S7.

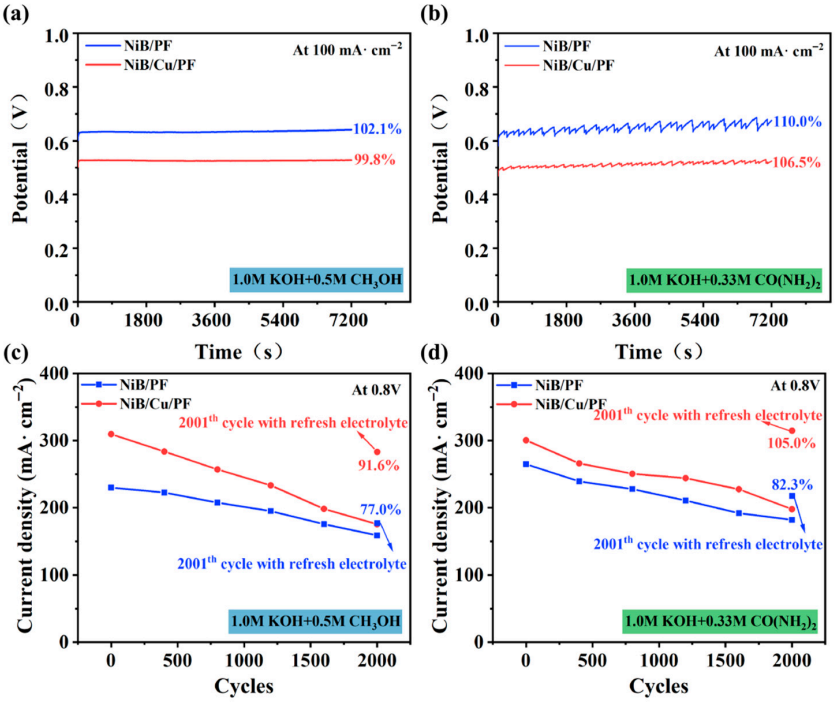


Figure 7. (**a**) Chronopotentiometry curves of NiB/PF and NiB/Cu/PF at 100 mA·cm^{-2} for 7200 s in 1.0 M KOH + 0.5 M CH_3OH and (**b**) 1.0 M KOH + 0.33 M $CO(NH_2)_2$. (**c**) Current density values (at 0.8 V) of NiB/PF and NiB/Cu/PF as a function of cycle number up to 2000 cycles in 1.0 M KOH + 0.5 M CH_3OH and (**d**) 1.0 M KOH + 0.33 M $CO(NH_2)_2$.

In addition, Figure 8 shows the SEM images of the two electrodes after 2000 CV cycles. In methanol solution, both electrodes maintain their morphology. In urea solution, the surface of NiB/PF shows obvious peeling, exposing the underlying fibers, while the surface of NiB/Cu/PF remained uniformly covered and structurally intact. These results further confirm that the Cu interlayer can enhance the adhesion between the NiB catalytic layer and the PF substrate, as well as improve the conductivity of the electrode, thereby effectively maintaining the structural integrity of the electrode under both MOR and UOR conditions, which is beneficial for achieving long-term electrochemical stability.

To evaluate the mechanical–electrochemical stability of the electrodes, repeated bending and twisting tests were performed on NiB/PF and NiB/Cu/PF electrodes. The mechanical bending and twisting tests were performed manually using tweezers to hold both ends of the electrode. For the bending test, the electrode was repeatedly bent to an angle of 180° and then returned to its original flat state. For the twisting test, the electrode was twisted by 360° along its longitudinal axis and then released back to the flat state. Each bending or twisting cycle was completed within approximately 1 s. Photographs of the test procedure are shown in Figure S8. The corresponding CV curves after bending and twisting cycles are provided in Figures S9 and S10, respectively. Figure 9a,b show the current density at 0.8 V as a function of bending and twisting cycles for the two electrodes in different test solutions. The results show that after bending and twisting, the performance of the NiB/Cu/PF electrode remains relatively stable, while the performance of the

NiB/PF electrode decreased significantly. Following the bending test, the current retention of NiB/Cu/PF is 96.7% in the methanol oxidation system and 84.6% in the urea oxidation system; for the twisting test, the values are 95.9% and 94.2%, respectively. In contrast, after bending, the current retentions of NiB/PF are 41.0% and 32.6%, and after twisting, they are only 13.3% and 12.6%, respectively, which further confirms the important role of the Cu interlayer in improving the mechanical stability of the electrodes.

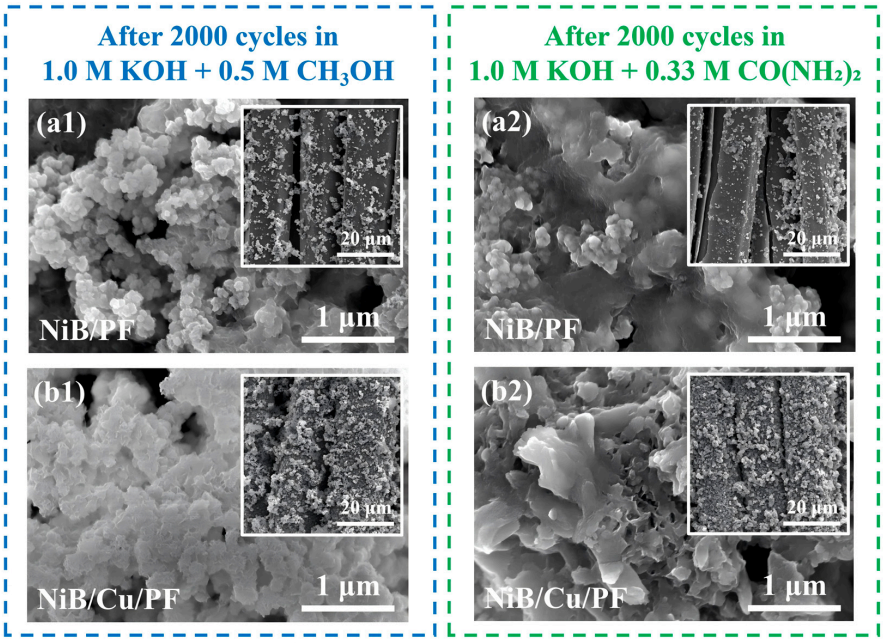


Figure 8. SEM images of NiB/PF and NiB/Cu/PF after 2000 cycles in (**a1**,**b1**) 1.0 M KOH + 0.5 M CH_3OH and (**a2**,**b2**) 1.0 M KOH + 0.33 M $CO(NH_2)_2$.

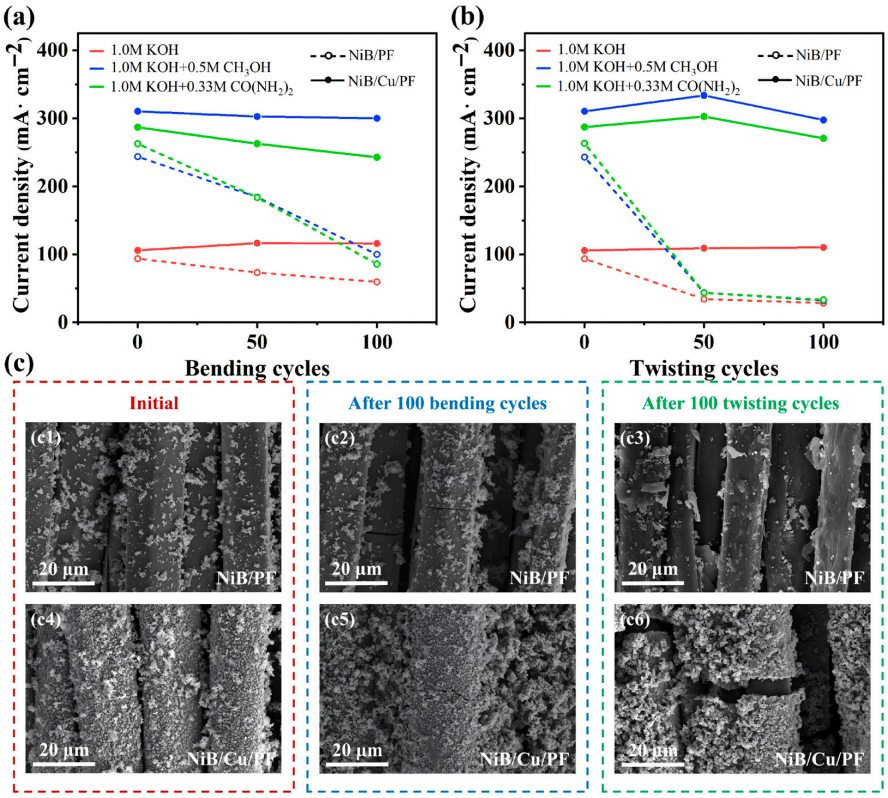


Figure 9. Current density at 0.8 V of NiB/PF and NiB/Cu/PF in different electrolytes after (**a**) bending and (**b**) twisting tests. (**c**) SEM images of (**c1**–**c3**) NiB/PF and (**c4**–**c6**) NiB/Cu/PF before and after 100 bending and twisting cycles.

Figure 9c shows the SEM images of the NiB/PF and NiB/Cu/PF electrodes before and after 100 bending and twisting cycles. After bending, the NiB/PF electrode exhibited wider and more numerous surface cracks compared to NiB/Cu/PF. After twisting, the NiB layer on NiB/PF underwent extensive delamination, whereas NiB/Cu/PF developed only localized microcracks and retained overall structural integrity. These results indicate that the Cu interlayer acts as a flexible stress buffer during mechanical deformation, effectively enhancing the adhesion between the coating and the substrate. Therefore, NiB/Cu/PF maintained good structural integrity and adhesion strength after bending and twisting, which is consistent with its stable performance observed in electrochemical tests [40].

4. Conclusions

In this study, waste polyester fabric (PF) was employed as a flexible substrate, and a NiB/Cu/PF composite electrode was fabricated via a two-step electroless plating process. The incorporation of the Cu interlayer markedly improved both electrolyte wettability and interfacial adhesion strength, thereby synergistically enhancing electrocatalytic activity, long-term electrochemical stability, and mechanical–electrochemical robustness. At 0.8 V, the NiB/Cu/PF electrode reaches average current densities of 312 mA·cm^{-2} for methanol oxidation (MOR) and 288 mA·cm^{-2} for urea oxidation (UOR), representing enhancements of 27.9% and 9.1%, respectively, over the NiB/PF electrode. Following accelerated durability testing (2000 CV cycles) and subsequent electrolyte replacement, NiB/Cu/PF retains 91.6% (MOR) and 105.0% (UOR) of its initial current density, whereas NiB/PF retains only 77.0% (MOR) and 82.3% (UOR), confirming good stability. Furthermore, the Cu interlayer significantly enhanced the mechanical–electrochemical stability of the electrode. After 100 bending cycles, the current density retentions of NiB/Cu/PF are 96.7% for MOR and 84.6% for UOR; After 100 twisting cycles, the values are 95.9% and 94.2%,

respectively. These findings demonstrate that the Cu interlayer functions as an effective stress-relieving interlayer, mitigating interfacial delamination and preserving electrical continuity during repeated deformation. This work establishes a waste-to-value strategy for upcycling discarded polyester fabric into high-performance flexible electrocatalysts with direct relevance to portable energy conversion systems and high-value utilization of waste.

Supplementary Materials: The following supporting information can be downloaded at: https://www.mdpi.com/article/10.3390/met16050528/s1, Figure S1: Schematic diagram of the test setup; Figure S2: High-resolution XPS spectrum of O1s; Figure S3: ECSA plots of (a) NiB/PF and (b) NiB/Cu/PF in 1.0 M KOH + 0.5 M CH_3OH and corresponding (c) Cdl data; ECSA plots of (d) NiB/PF and (e) NiB/Cu/PF in 1.0 M KOH + 0.33 M $CO(NH_2)_2$ and corresponding (f) Cdl data; Figure S4: Tafel slopes of NiB/PF and NiB/Cu/PF electrodes in (a) 1.0 M KOH + 0.5 M CH_3OH and (b) 1.0 M KOH + 0.33 M $CO(NH_2)_2$; Figure S5: CV curves of Cu/PF with different electroless plating times in (a) 1 M KOH, (b) 1.0 M KOH + 0.5 M CH_3OH, and (c) 1.0 M KOH + 0.33 M $CO(NH_2)_2$, and (d) the peak current densities in different electrolytes at 0.8 V; Figure S6: CV curves of NiB/Cu/PF with different B contents in (a) 1 M KOH, (b) 1.0 M KOH + 0.5 M CH_3OH, and (c) 1.0 M KOH + 0.33 M $CO(NH_2)_2$; Figure S7: CV curves of NiB/PF before and after 2000 cycles and the 2001st cycle in (a) 1.0 M KOH + 0.5 M CH_3OH and (b) 1.0 M KOH + 0.33 M $CO(NH_2)_2$; CV curves of NiB/Cu/PF before and after 2000 cycles and the 2001st cycle in (c) 1.0 M KOH + 0.5 M CH_3OH and (d) 1.0 M KOH + 0.33 M $CO(NH_2)_2$; Figure S8: Images of NiB/Cu/PF during (a1) bending and (a2) twisting tests; Figure S9: CV curves of NiB/PF after 0, 50, and 100 bending cycles in (a1) 1.0 M KOH, (a2) 1.0 M KOH + 0.5 M CH_3OH, and (a3) 1.0 M KOH + 0.33 M $CO(NH_2)_2$; CV curves of NiB/Cu/PF after 0, 50, and 100 bending cycles in (b1) 1.0 M KOH, (b2) 1.0 M KOH + 0.5 M CH_3OH, and (b3) 1.0 M KOH + 0.33 M $CO(NH_2)_2$; Figure S10: CV curves of NiB/PF after 0, 50, and 100 twisting cycles in (a1) 1.0 M KOH, (a2) 1.0 M KOH + 0.5 M CH_3OH, and (a3) 1.0 M KOH + 0.33 M $CO(NH_2)_2$; CV curves of NiB/Cu/PF after 0, 50, and 100 twisting cycles in (b1) 1.0 M KOH, (b2) 1.0 M KOH + 0.5 M CH_3OH, and (b3) 1.0 M KOH + 0.33 M $CO(NH_2)_2$; Table S1: Comparison of electro-oxidation performance of Ni-based electrodes for methanol and urea; Table S2: XPS-derived surface atomic percentages of the NiB/Cu/PF electrode. References [41–48] are cited in the Supplementary Materials.

Author Contributions: Conceptualization, Validation, Investigation, Data curation, Writing—original draft, G.H.; Validation, Investigation, Data curation, Consulted the literature, Writing, S.C.; Writing—review and editing, Supervision, J.Z.; Writing—review and editing, Supervision, Q.C.; Conceptualization, Resources, Writing—review and editing, Supervision, Project administration, Funding acquisition, Y.T. All authors have read and agreed to the published version of the manuscript.

Funding: This research was funded by the Zhejiang Provincial Natural Science Foundation of China, grant number LY23E010008, and by the National Natural Science Foundation of China, grant number 520023158.

Data Availability Statement: The original contributions presented in this study are included in the article/Supplementary Material. Further inquiries can be directed to the corresponding authors.

Conflicts of Interest: The authors declare no conflicts of interest.

References

1. Cai, M.; Zhang, Y.; He, P.; Zhang, Z. Recent Advances in Revealing the Electrocatalytic Mechanism for Hydrogen Energy Conversion System. *Small* **2024**, *20*, 2405008. [CrossRef]
2. Wang, J.; Zhang, B.; Guo, W.; Wang, L.; Chen, J.; Pan, H.; Sun, W. Toward Electrocatalytic Methanol Oxidation Reaction: Longstanding Debates and Emerging Catalysts. *Adv. Mater.* **2023**, *35*, 2211099. [CrossRef]
3. Li, J.; Li, L.; Wang, J.; Cabot, A.; Zhu, Y. Boosting hydrogen evolution by methanol oxidation reaction on Ni-based electrocatalysts: From fundamental electrochemistry to perspectives. *ACS Energy Lett.* **2024**, *9*, 853–879. [CrossRef]
4. Gao, X.; Zhang, S.; Wang, P.; Jaroniec, M.; Zheng, Y.; Qiao, S.Z. Urea catalytic oxidation for energy and environmental applications. *Chem. Soc. Rev.* **2024**, *53*, 1552–1591. [CrossRef]

5. Zhu, D.; Zhang, H.; Miao, J.; Hu, F.; Wang, L.; Tang, Y.; Qiao, M.; Guo, C. Strategies for designing more efficient electrocatalysts towards the urea oxidation reaction. *J. Mater. Chem. A* **2022**, *10*, 3296–3313. [CrossRef]
6. Xu, S.; Ruan, X.; Ganesan, M.; Wu, J.; Ravi, S.K.; Cui, X. Transition metal-based catalysts for urea oxidation reaction (UOR): Catalyst design strategies, applications, and future perspectives. *Adv. Funct. Mater.* **2024**, *34*, 2313309. [CrossRef]
7. Li, J.; Zhang, J.; Yang, J.H. Research progress and applications of nickel-based catalysts for electrooxidation of urea. *Int. J. Hydrogen Energy* **2022**, *47*, 7693–7712. [CrossRef]
8. Gautam, J.; Lee, S.Y.; Park, S.J. Cutting-edge optimization strategies and in situ characterization techniques for urea oxidation reaction catalysts: A comprehensive review. *Adv. Energy Mater.* **2025**, *15*, 2406047. [CrossRef]
9. Hu, Y.; Shao, L.; Jiang, Z.; Shi, L.; Li, Q.; Shu, K.; Chen, H.; Li, G.; Dong, Y.; Wang, T.; et al. Unveiling the role of boron on nickel-based catalyst for efficient urea oxidation assisted hydrogen production. *Adv. Funct. Mater.* **2024**, *34*, 2411011. [CrossRef]
10. Huang, T.; Shen, T.; Gong, M.; Deng, S.; Lai, C.; Liu, X.; Zhao, T.; Teng, L.; Wang, D. Ultrafine Ni-B nanoparticles for efficient hydrogen evolution reaction. *Chin. J. Catal.* **2019**, *40*, 1867–1873. [CrossRef]
11. Baloyi, R.B.; Gbadeyan, O.J.; Sithole, B.; Chunilall, V. Recent advances in recycling technologies for waste textile fabrics: A review. *Text. Res. J.* **2024**, *94*, 508–529. [CrossRef]
12. Qiu, T.; Halpern, B.; Maslennikov, A.; Rawat, M.; Halanur, M.; Mamane, H. Valorization of post-consumer cotton-rich textile waste into cellulose nanocrystals via sulfuric acid hydrolysis and ozone-assisted bleaching. *Chem. Eng. J.* **2025**, *528*, 172340. [CrossRef]
13. Leenders, N.; Moerbeek, R.M.; Puijk, M.J.; Bronkhorst, R.J.A.; Bueno Morón, J.; van Klink, G.P.M.; Gruter, G.-J.M. Polycotton waste textile recycling by sequential hydrolysis and glycolysis. *Nat. Commun.* **2025**, *16*, 738. [CrossRef]
14. Zhang, W.; Xi, R.; Li, Y.; Zhang, Y.; Wang, P.; Hu, D. Waste silk fabric derived N-doped carbon as a self-supported electrocatalyst for hydrogen evolution reaction. *Colloids Surf. A* **2023**, *658*, 130704. [CrossRef]
15. Jiang, S.; Shao, H.; Cao, G.; Li, H.; Xu, W.; Li, J.; Fang, J.; Wang, X. Waste cotton fabric derived porous carbon containing Fe_3O_4/NiS nanoparticles for electrocatalytic oxygen evolution. *J. Mater. Sci. Technol.* **2020**, *59*, 92–99. [CrossRef]
16. Darvishzadeh, A.; Nasouri, K. Manufacturing, modeling, and optimization of nickel-coated carbon fabric for highly efficient EMI shielding. *Surf. Coat. Technol.* **2021**, *414*, 126957. [CrossRef]
17. Moazzenchi, B.; Montazer, M. Copper Sonosensitization and Nickel Electroless Sonoplating on Polyester Fabric Generating Conductive, Magnetic and Antibacterial Properties. *Fibers Polym.* **2021**, *22*, 2678–2687. [CrossRef]
18. Chang, W.; Nam, D.; Lee, S.; Ko, Y.; Kwon, C.H.; Ko, Y.; Cho, J. Fibril-type textile electrodes enabling extremely high areal capacity through pseudocapacitive electroplating onto chalcogenide nanoparticle-encapsulated fibrils. *Adv. Sci.* **2022**, *9*, 2203800. [CrossRef] [PubMed]
19. Kim, T.; Park, C.; Samuel, E.P.; Kim, Y.-I.; An, S.; Yoon, S.S. Wearable sensors and supercapacitors using electroplated-Ni/ZnO antibacterial fabric. *J. Mater. Sci. Technol.* **2022**, *100*, 254–264. [CrossRef]
20. He, R.; Li, J.; Chen, M.; Zhang, S.; Cheng, Y.; Ning, X.; Wang, N. Tailoring moisture electroactive Ag/Zn@ cotton coupled with electrospun PVDF/PS nanofibers for antimicrobial face masks. *J. Hazard. Mater.* **2022**, *428*, 128239. [CrossRef]
21. Wang, W.; Jiang, Z.; Tian, X.; Maiyalagan, T.; Jiang, Z.J. Self-standing CoFe embedded nitrogen-doped carbon nanotubes with Pt deposition through direct current plasma magnetron sputtering for direct methanol fuel cells applications. *Carbon* **2023**, *201*, 1068–1080. [CrossRef]
22. Liu, M.; Yang, Y.; Liu, R.; Wang, K.; Cheng, S.; Yuan, H.; Huang, K.; Liang, F.; Yang, F.; Zheng, K.; et al. Carbon Nanotubes/Graphene-Skinned Glass Fiber Fabric with 3D Hierarchical Electrically and Thermally Conductive Network. *Adv. Funct. Mater.* **2024**, *34*, 2409379. [CrossRef]
23. Xie, Y.; Liu, S.; Huang, K.; Chen, B.; Shi, P.; Chen, Z.; Liu, B.; Liu, K.; Wu, Z.; Chen, K.; et al. Ultra-Broadband Strong Electromagnetic Interference Shielding with Ferromagnetic Graphene Quartz Fabric. *Adv. Mater.* **2022**, *34*, 2202982. [CrossRef] [PubMed]
24. Luo, Z.; Han, P.; Yu, B.; Yan, W.; Chen, X.; Feng, Y.; Zheng, H.; Guo, H.; Cheng, Z.; He, J. RGO/ANFs composite fibers with dual functions of thermal conductivity and electromagnetic shielding of lotus root structure based on sol-gel wet spinning. *Carbon* **2024**, *226*, 119142. [CrossRef]
25. Singh, M.; Kafle, A.; Gupta, D.; Nagaiah, T.C. Long Life with Ultrahigh Capacitance Flexible Electrode At Practical Mass Loading For Battery Supercapacitor Hybrid. *Small* **2025**, *21*, e08953. [CrossRef]
26. Yu, W.; Wei, Z.; Wang, L.; Shang, J.; Xu, H.; Luo, Y.; Cai, J.; Xie, C.; Guo, Y.; Zhou, J.; et al. Surface-Stabilized and Lightweight Metallic PET Fabrics for Flexible and Energy-Dense Li-Ion Batteries. *Adv. Sci.* **2025**, *12*, e13494. [CrossRef] [PubMed]
27. He, D.; Qin, H.; Qian, L.; Sun, L.; Li, J. Conductive Chitosan Nonwoven Fabrics by Electroless Plating with Excellent Laundering Durability for Wearable Electronics. *J. Nat. Fibers* **2022**, *20*, 14855–14865. [CrossRef]
28. Park, J.-H.; Park, J.; Tang, F.; Song, Y.-G.; Jeong, Y.G. Electromagnetic Interference Shielding and Joule Heating Properties of Flexible, Lightweight, and Hydrophobic MXene/Nickel-Coated Polyester Fabrics Manufactured by Dip-Dry Coating and Electroless Plating. *ACS Appl. Mater. Interfaces* **2024**, *16*, 38490–38500. [CrossRef]

29. Sharma, P.J.; Modi, K.H.; Sahatiya, P.; Sumesh, C.K.; Pataniya, P.M. Electroless deposited NiP-fabric electrodes for efficient water and urea electrolysis for hydrogen production at industrial scale. *Appl. Surf. Sci.* **2024**, *644*, 158766. [CrossRef]
30. Wang, D.; Sun, J.; Xue, Q.; Li, Q.; Guo, Y.; Zhao, Y.; Chen, Z.; Huang, Z.; Yang, Q.; Liang, G.; et al. A universal method towards conductive textile for flexible batteries with superior softness. *Energy Storage Mater.* **2021**, *36*, 272–278. [CrossRef]
31. Khajeh, E.; Nasouri, K.; Askari, G.; Mandegari, M. Flexible and lightweight metalized polyamide nonwoven for electromagnetic interference shielding, electrothermal, photothermal, and antibacterial applications. *Chem. Eng. J.* **2024**, *502*, 158203. [CrossRef]
32. Ko, Y.; Hinestroza, J.P.; Uyar, T. Structural Investigation on Electrospun Nanofibers from Postconsumer Polyester Textiles and PET Bottles. *ACS Appl. Polym. Mater.* **2023**, *5*, 7298–7307. [CrossRef]
33. Dai, W.; Li, H.; Cao, Y.; Qiao, M.; Fan, K.; Deng, J. Evidence for the Antioxidation Effect of Boron on the Ultrafine Amorphous Ni−B Alloy Catalyst. *Langmuir* **2002**, *18*, 9605–9608. [CrossRef]
34. Grosvenor, A.P.; Biesinger, M.C.; Smart, R.S.C.; McIntyre, N.S. New interpretations of XPS spectra of nickel metal and oxides. *Surf. Sci.* **2006**, *600*, 1771–1779. [CrossRef]
35. Xu, J.; Gong, X.; Meng, Z.; Chen, P.; Nan, H.; Li, Y.; Deng, T.; Wang, D.; Zeng, Y.; Hu, X.; et al. Bi-Interlayer Strategy for Modulating NiCoP-Based Heterostructure toward High-Performance Aqueous Energy Storage Devices. *Adv. Mater.* **2024**, *36*, 2401452. [CrossRef] [PubMed]
36. Sun, Y.; Cao, W.; Ge, X.; Yang, X.; Wang, Y.; Xu, Y.; Ouyang, B.; Shen, Q.; Li, C. Built-in electric field induced interfacial charge distributions of $Ni_2P/NiSe_2$ heterojunction for urea-assisted hydrogen evolution reaction. *Inorg. Chem. Front.* **2023**, *10*, 6674–6682. [CrossRef]
37. Zago, S.; Scarpetta-Pizo, L.C.; Zagal, J.H.; Specchia, S. PGM-Free Biomass-Derived Electrocatalysts for Oxygen Reduction in Energy Conversion Devices: Promising Materials. *Electrochem. Energy Rev.* **2024**, *7*, 1. [CrossRef]
38. Luo, X.; Gan, Y.; Yang, X.; Wang, Y.; Yang, H.; Dai, Z.; Zhu, Z.; Tian, Y.; Jiang, L. Balance of electroplating and electrophoresis for construction of robust photocatalytic copper–titanium dioxide composite coating. *Adv. Mater. Interfaces* **2025**, *12*, 2401022. [CrossRef]
39. Chen, J.; Chen, H.; Yin, H.; He, H.; Wang, Z.; Yu, D.; Liang, J.; Huang, Y.; Qin, L.; Chen, D. Understanding the promotion mechanism of boron during the surface reconstruction of Ni_2B nanoflakes for efficient urea electrocatalytic oxidation. *Chem. Eng. J.* **2023**, *477*, 146885. [CrossRef]
40. Nagaraju, G.; Chandra Sekhar, S.; Krishna Bharat, L.; Yu, J.S. Wearable Fabrics with Self-Branched Bimetallic Layered Double Hydroxide Coaxial Nanostructures for Hybrid Supercapacitors. *ACS Nano* **2017**, *11*, 10860–10874. [CrossRef]
41. Jia, F.; Wang, X.; Guo, H.; Wu, N.; Zhao, Y.; Li, Y.; He, J.; Yang, S. In situ growth of Ni/Ni_3S_2–MoO_2 nanocrystals on carbon cloth for the enhanced electrocatalytic oxidation of methanol. *Appl. Surf. Sci.* **2023**, *640*, 158348. [CrossRef]
42. Rajpure, M.; Jadhav, H.; Kim, H. Advanced LDH-MOF derived bimetallic NiCoP electrocatalyst for methanol oxidation reaction. *Colloids Surf. A* **2022**, *654*, 130062. [CrossRef]
43. Cheng, J.; Liu, X.; Yang, J.; Liu, J.; Zhang, L.; Zhang, L. Three-dimensional Ni-MoN nanorod array as active and non-precious metal electrocatalyst for methanol oxidation reaction. *Electroanal. Chem.* **2022**, *906*, 116001. [CrossRef]
44. Chen, F.; Ho, Y.; Chang, H.; Tsai, Y. Nanocomposite integrating tube-like $NiCo_2S_4$ and carbon nanotubes for electrooxidation of methanol. *Electrochem. Commun.* **2020**, *117*, 106783. [CrossRef]
45. Chen, L.; Wang, L.; Ren, J.-T.; Wang, H.-Y.; Tian, W.-W.; Sun, M.-L.; Yuan, Z.-Y. Artificial Heterointerfaces with Regulated Charge Distribution of Ni Active Sites for Urea Oxidation Reaction. *Small Methods* **2024**, *8*, e2400108. [CrossRef] [PubMed]
46. Sayed, E.T.; Alami, A.H.; Abdelkareem, M.A.; Wilberforce, T.; Kamarudin, S.K.; Olabi, A.G. Real direct urea fuel cell operation using standalone Ni-based metal-organic framework prepared by ball mill at room temperature. *Energy* **2024**, *305*, 132164. [CrossRef]
47. Chen, L.; Wang, P.; Wang, L.; Ren, J.-T.; Wang, H.-Y.; Tian, W.-W.; Sun, M.-L.; Yuan, Z.-Y. Insights into the Understanding of the Nickel-Based Pre-Catalyst Effect on Urea Oxidation Reaction Activity. *Molecules* **2024**, *29*, 3321.
48. Wu, N.; Guo, R.; Zhang, X.; Gao, N.; Chi, X.; Cao, D.; Hu, T. Nickel/nickel oxide nanocrystal nitrogen-doped carbon composites as efficient electrocatalysts for urea oxidation. *J. Alloys Compd.* **2021**, *870*, 159408. [CrossRef]

Disclaimer/Publisher's Note: The statements, opinions and data contained in all publications are solely those of the individual author(s) and contributor(s) and not of MDPI and/or the editor(s). MDPI and/or the editor(s) disclaim responsibility for any injury to people or property resulting from any ideas, methods, instructions or products referred to in the content.